Monthly Notices of the ROYAL ASTRONOMICAL SOCIETY

MNRAS **524,** 1601–1614 (2023) https://doi.org/10.1093/mnras/stad1915
Advance Access publication 2023 June 29

NGC 2022, a case study of a multiple-shell planetary nebula

B. Montoro-Molina,[1★] M. A. Guerrero ,[1★] E. Santamaría,[2,3] J. A. Toalá,[4] Y.-H. Chu,[5]
G. Ramos-Larios ,[2,3] R. Infante-Sainz ,[6] M. Akhlaghi,[6] S. Eskandarlou[6] and C. López-Sanjuan[6]

[1]*Instituto de Astrofísica de Andalucía, IAA-CSIC, Glorieta de la Astronomía S/N, Granada E-18008, Spain*
[2]*Universidad de Guadalajara, CUCEI, Blvd. Marcelino García Barragán 1421, 44430 Guadalajara, Jalisco, Mexico*
[3]*Instituto de Astronomía y Meteorología, Dpto. de Física, CUCEI, Av. Vallarta 2602, 44130 Guadalajara, Jalisco, Mexico*
[4]*Instituto de Radioastronomía y Astrofísica, UNAM, Ant. Carretera a Pátzcuaro 8701, Ex-Hda. San José de la Huerta, Morelia 58089, Mich., Mexico*
[5]*Institute of Astronomy and Astrophysics, Academia Sinica (ASIAA), No. 1, Section 4, Roosevelt Road, Taipei 10617, Taiwan*
[6]*Centro de Estudios de Física del Cosmos de Aragón (CEFCA), Plaza San Juan 1, E-44001 Teruel, Spain*

Accepted 2023 June 21. Received 2023 June 21; in original form 2023 April 21

ABSTRACT

We present a detailed study of the physical properties, history of mass loss, and chemical abundances of the planetary nebula NGC 2022. New imaging observations obtained with the OAJ/JAST80 and NOT/ALFOSC confirm the presence of a faint ∼88 arcsec halo surrounding a double-layered elliptical structure that consists of a bright 21.4 × 16.7 arcsec inner shell and a 32 arcsec diameter envelope. The long-slit high-dispersion echelle observations obtained with MES on the OAN-SPM 2.1-m telescope can be well described by a SHAPE model with expansion velocities of 43 ± 3 and 34 ± 3 km s^{-1} along the major and minor axes of the elliptical inner shell, respectively. In addition, a deep long-slit high-dispersion echelle observation made with the KPNO 4-m telescope detected line-splitting in the faint halo, revealing an expansion velocity of 15.5 ± 2 km s^{-1}. We have also used new intermediate-dispersion optical spectra with the NOT, complemented with *IUE* data, to study the chemical abundances of each shell. The abundances of the three shells are typical of a Type II in the Peimbert classification of PNe and do not exhibit any notable anomalies. Finally, we estimate the total mass of NGC 2022 to be ≈0.9 M$_\odot$, which consists of 0.64 M$_\odot$ from the CSPN and 0.1, 0.11, and 0.1 × $f_{\rm halo}^{1/2}$ M$_\odot$ from the ionized inner shell, outer shell, and halo, respectively.

Key words: stars: evolution – (ISM:) planetary nebulae: general – (ISM:) planetary nebulae: individual: (NGC 2022).

1 INTRODUCTION

Planetary nebulae (PNe) consist of the stellar material ejected by evolved low- and intermediate-mass stars before they turn into white dwarfs (WDs). A wide variety of morphology has been observed in PNe. Their overall shapes can be elliptical or bipolar, and they may appear single-shelled or multiple-shelled (Balick 1987; Chu, Jacoby & Arendt 1987, hereafter CJA87). The morphology and radial extent of a PN are determined by the prolonged history of stellar mass loss, which in turn depends on the mass and binarity of the central star. While *Hubble Space Telescope* (*HST*) images have resolved detailed structures in PNe, deep ground-based images have otherwise revealed faint, extended structures outside their main nebulae (e.g. Corradi et al. 2003). To investigate the complete mass loss history of the central star of a PN (CSPN), it is thus necessary to take into account the features observed at all spatial scales in the PN.

PNe have been observed by ground-based telescopes in optical wavelengths as well as space-based telescopes in IR/UV/X-ray wavelengths. The archived data of PN observations at multi-wavelengths provides an excellent opportunity to comprehensively analyse PNe and derive the physical properties and mass loss history of CSPNs. In this paper, we use NGC 2022 to showcase such a study.

NGC 2022 is a multiple-shell PN at a distance of $2.10^{+0.25}_{-0.15}$ kpc (see Bailer-Jones et al. 2021). Its central star has been reported to have an effective temperature ($T_{\rm eff}$) of 100 000 K and a log g of 5.3 dex (McCarthy, Mendez & Kudritzki 1997). The multiple-shell morphology of NGC 2022 has been described by CJA87 to have a bright 21 × 17 arcsec inner shell enveloped by an attached 32 arcsec in diameter outer shell that is well developed in all directions except the poles of the inner shell's major axis (a CJA87 Type IIc PN), as well as a faint halo (Type I according to CJA87) about 88 arcsec in size. The bright main nebula's inner and outer shells have also been called 'core' and 'rim' by Balick (1987). The expansion velocity of the bright inner shell has been measured to be 28 ± 2 km s^{-1}, while the outer shell expands more slowly (Sabbadin, Bianchini & Hamzaoglu 1984).

In order to make a comprehensive study of NGC 2022, we have collected available archival data at multiple wavelengths, including our own unpublished data, and made complementary new observations. These data are used here to analyse the physical structure of this PN from the bright inner shell to the faint halo. We further use 3D models to reproduce the nebular morphology and kinematics. We have also used stellar photometry and nebular abundances and kinematics to assess the physical prop-

★ E-mail: borjamm@iaa.es (BMM); mar@iaa.es (MAG)

erties of the CSPN. This paper reports our analysis and results of NGC 2022.

2 OBSERVATIONS AND DATA REDUCTION

2.1 Imaging

Broad-band *HST* images of NGC 2022 taken with the Wide-Field Camera of the Advanced Camera for Surveys (ACS/WFC) on 2009 August 7 (Prop.ID. 11599, PI: R. Wade) were downloaded from the Barbara A. Mikulski Archive for Space Telescopes (MAST).[1] The images were acquired using the *F*555*W* and *F*814*W* filters for total exposure times of 600 and 270 s, respectively. These images have been used to produce the colour-composite picture presented in the top left-hand panel of Fig. 1.

Narrow-band images of NGC 2022 in the Hα and [O III] emission lines were acquired with the 2.56-m Nordic Optical Telescope (NOT) of the Observatorio de El Roque de los Muchachos (ORM, La Palma, Spain) on 2014 March 8, using the Alhambra Faint Object Spectrograph and Camera (ALFOSC)[2] with the NOT #64 (Halp 656_5) and #90 ([O III] 501_3) filters, respectively.

In each filter, two 1200 s exposures were made, resulting in a total exposure of 2400 s. The images were bias-subtracted and flat-fielded using suitable sky flat fields obtained at sunset on the same night. The pixel scale is 0.190 arcsec pix^{-1} and the spatial resolution, estimated from the FWHM of stars in the field of view (FoV), is 1.4 arcsec in the Hα image and 1.2 arcsec in the [O III] image. The NOT Hα and [O III] images and a colour-composite picture made with these two images and an image obtained through a Sloan Digital Sky Survey (SDSS) *r* filter are also shown in Fig. 1.

Broad-band SDSS *g*, wide-field images of NGC 2022 were obtained with the T80Cam instrument (Marin-Franch et al. 2015) mounted on the 80-cm Javalambre Auxiliary Survey Telescope (JAST80) at the Observatorio Astrofísico de Javalambre (OAJ, Cenarro et al. 2014). The T80Cam camera uses a back-illuminated e2v CCD290-99 9.2 × 9.2 K CCD, providing a pixel scale of 0.55 arcsec pix^{-1} and a FoV of 1.4° × 1.4°. To search for extended low-surface brightness emission around the main nebula of NGC 2022, twenty-five 120 s exposures were obtained on 2022 September 29 and seventy-five 120 s exposures on 2022 October 20. These imaging observations followed a 5 × 5 dithering pattern with 15 arcmin offsets. The images were flat-fielded, aligned, and then combined for a total exposure time of 12 000 s. The multipointing images ensure the flatness of the background emission. The spatial resolution of the final image, as derived from the FWHM of stars in the FoV, is 1.8 arcsec.

To illustrate all the morphological features of NGC 2022 in one picture, we have adopted the best large-scale [O III] image taken with the Issac Newton Telescope Wide Field Camera (INT WFC; Corradi et al. 2003), filled the gaps with our NOT [O III] image, replaced the central region with the *HST* colour composite image. The resulting picture is shown in Fig. 2.

2.2 Intermediate-dispersion spectroscopy

Intermediate-resolution long-slit spectroscopic observations of NGC 2022 were made on 2022 March 2 using ALFOSC at the NOT of the ORM. The observations consisted of three 1500 s exposures acquired using the grism #7, which provided a spectral scale of 1.68 Å pix^{-1} and a spectral coverage of 3650–7110 Å. The slit width was set to 1 arcsec, resulting in a spectral resolution ≈8.2 Å. The slit was placed at an angle of 40° across the central star, as shown in the bottom left-hand panel of Fig. 1.

The raw data were reduced using standard IRAF[3] (Tody 1993) tasks to subtract the bias and to apply the flat-field correction. The wavelength calibration was carried out using ThAr and Ne arc lamps. The flux calibration was made using observations of the spectrophotometric standard star Feige 34 obtained in the same night. It should be mentioned that since one of our objectives was the detection of emission lines from the low-surface brightness nebular halo, special attention was paid to the sky subtraction to avoid removing emission from that nebular region.

2.3 Archival *IUE* UV spectroscopy

NGC 2022 has a high ionization state, as its CSPN has a $T_{\rm eff}$ of $\sim 10^5$ K (McCarthy et al. 1997) and high-excitation nebular emission lines are detected in our intermediate-resolution optical spectra. An appropriate determination of the nebular abundance should take into account the well known high-excitation ions, whose emission lines are observable in the UV spectral range. Thus, we retrieved low-resolution (6 Å) UV short-wave (SW) and long-wave (LW) spectra that cover spectral ranges of 1150–2000 and 1850–3000 Å, respectively, from the *International Ultraviolet Explorer* (*IUE*) New Extracted Spectra (INES)[4] compiled by Barbara A. Milkuski. The sequence numbers and dates of observation (in parentheses) of the IUE data used are SWP08676LL (1980 Apr 5), SWP32729LL (1988 Jan 13), SWP32732LL (1988 Jan 14), SWP38320LL (1990 March 7), SWP38321LL (1990 Mar 8), LWR07428LL (1980 Apr 5), LWP04612LL (1984 Oct 22), LWP04621LL (1984 Oct 23), and LWP17502LL (1990 Mar 8). The suffix 'LL' of the sequence number stands for large aperture and low dispersion. The 10 × 23 arcsec aperture used in these observations was centred on the CSPN and was large enough to include the bulk of the bright inner shell of NGC 2022; thus, the spectra contained both emission lines from the nebula and the continuum of the CSPN.

2.4 High-dispersion spectroscopy

Long-slit high-dispersion spectroscopic observations of NGC 2022 were obtained using the Manchester Echelle Spectrometer (MES; Meaburn et al. 2003) mounted on the 2.1-m telescope at the Observatorio Astronómico Nacional in San Pedro Mártir (OAN-SPM, Mexico)[5] and the echelle spectrograph on the Mayall 4-m Telescope at the Kitt Peak National Observatory (KPNO).

The SPM MES observations were conducted on 2022 April 3 and 2022 October 24 (see Table 1). The E2V 42-40 CCD with pixel size 13.5 µm was used with 2 × 2 and 4 × 4 on-chip binning, resulting in a plate scale of 0.351 arcsec and 0.702 arcsec pix^{-1}, respectively. To avoid overlapping orders in long-slit observations, a broad Hα

[1] https://mast.stsci.edu/
[2] http://www.not.iac.es/instruments/alfosc/

[3] IRAF was distributed by the National Optical Astronomy Observatory, which was operated by the Association of Universities for Research in Astronomy (AURA) under a cooperative agreement with the National Science Foundation.
[4] http://sdc.cab.inta-csic.es/ines/
[5] The Observatorio Astronómico Nacional at the Sierra de San Pedro Mártir (OAN-SPM) is operated by the Instituto de Astronomía of the Universidad Nacional Autónoma de México.

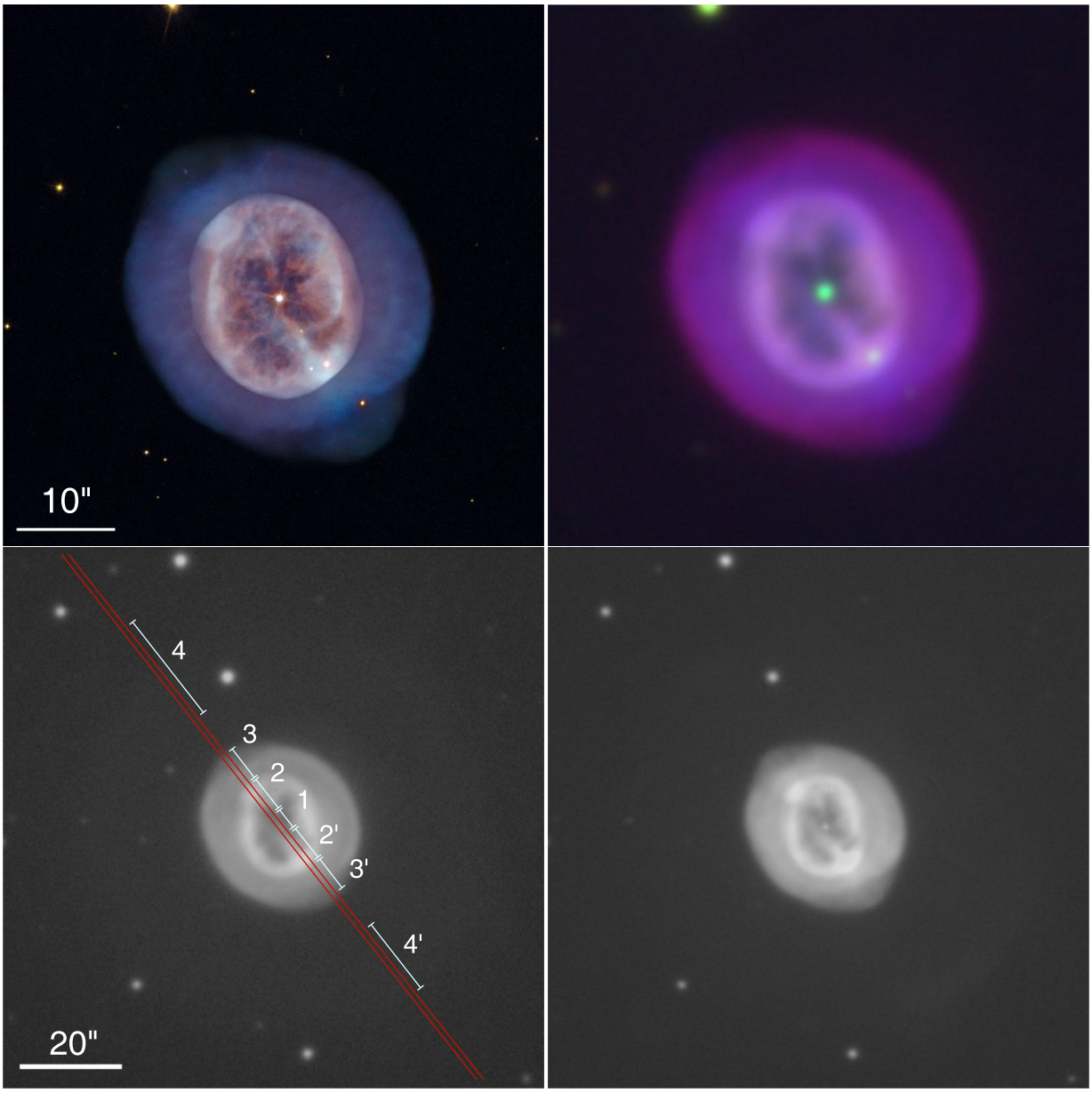

Figure 1. Images of the brightest nebular shells of NGC 2022. (top-left) *HST* ACS/WFC *F*555*W* (blue + green) and *F*814*W* (red) colour-picture revealing the fine details of the inner shell and envelope. (top-right) NOT ALFOSC Hα (red), [O III] (blue), and *r*-SDSS (green) colour-composite picture showing the ionization structure of the main shell. (bottom) NOT ALFOSC Hα (left) and [O III] (right) images with a larger field of view. The Hα image is overlaid by a 1 arcsec wide slit (red), together with the four spectral apertures (white) used to extract 1D spectra for the star (#1), inner shell (#2, #2 arcmin), envelope (#3, #3 arcmin), and halo (#4, #4 arcmin).

filter ($\Delta\lambda = 90$ Å) was used to isolate the 87th echelle order, where the spectral reciprocal dispersion was 0.050 and 0.10 Å pix^{-1} for the 2 × 2 and 4 × 4 binning, respectively. Similarly, an [O III] λ5007 Å filter ($\Delta\lambda = 50$ Å) was used to isolate the 114th echelle order, where the spectral reciprocal dispersion was 0.043 and 0.086 Å pix^{-1} for the 2 × 2 and 4 × 4 binning, respectively.

The KPNO echelle observations were conducted with the Mayall 4-m Telescope on 1984 March 25 and 1987 September 2 (see Table 1). The 800 × 800 TI2 CCD with pixel size 15 µm was used with a 2 × 2 on-chip binning, resulting in a plate scale of 0.33 arcsec pix^{-1}. The 79 line mm^{-1} echelle grating and the long-focus camera were used, providing a spectral reciprocal dispersion of 2.47 Å mm^{-1}, i.e. 0.074 Å for each binned pixel. A detailed description of the observing configuration has been reported by Chu et al. (1991).

In this paper, we will use the echellograms obtained with longslits going through the CSPN along PA 37° and along the North–South direction offset 20 arcsec west of the CSPN.

The spectra were processed using IRAF standard calibration routines, including bias subtraction, flat-fielding by quartz lamp observations in the beginning of night, and curvature correction and wavelength calibration with ThAr arc lamp observations obtained immediately before and/or after the science observations. The wavelength accuracy is estimated to be ± 1 km s^{-1}. The instrumental FWHM for the SPM MES 2 × 2 and 4 × 4 binning observations are 5.1 ± 0.3 and 12.2 ± 0.7 km s^{-1},

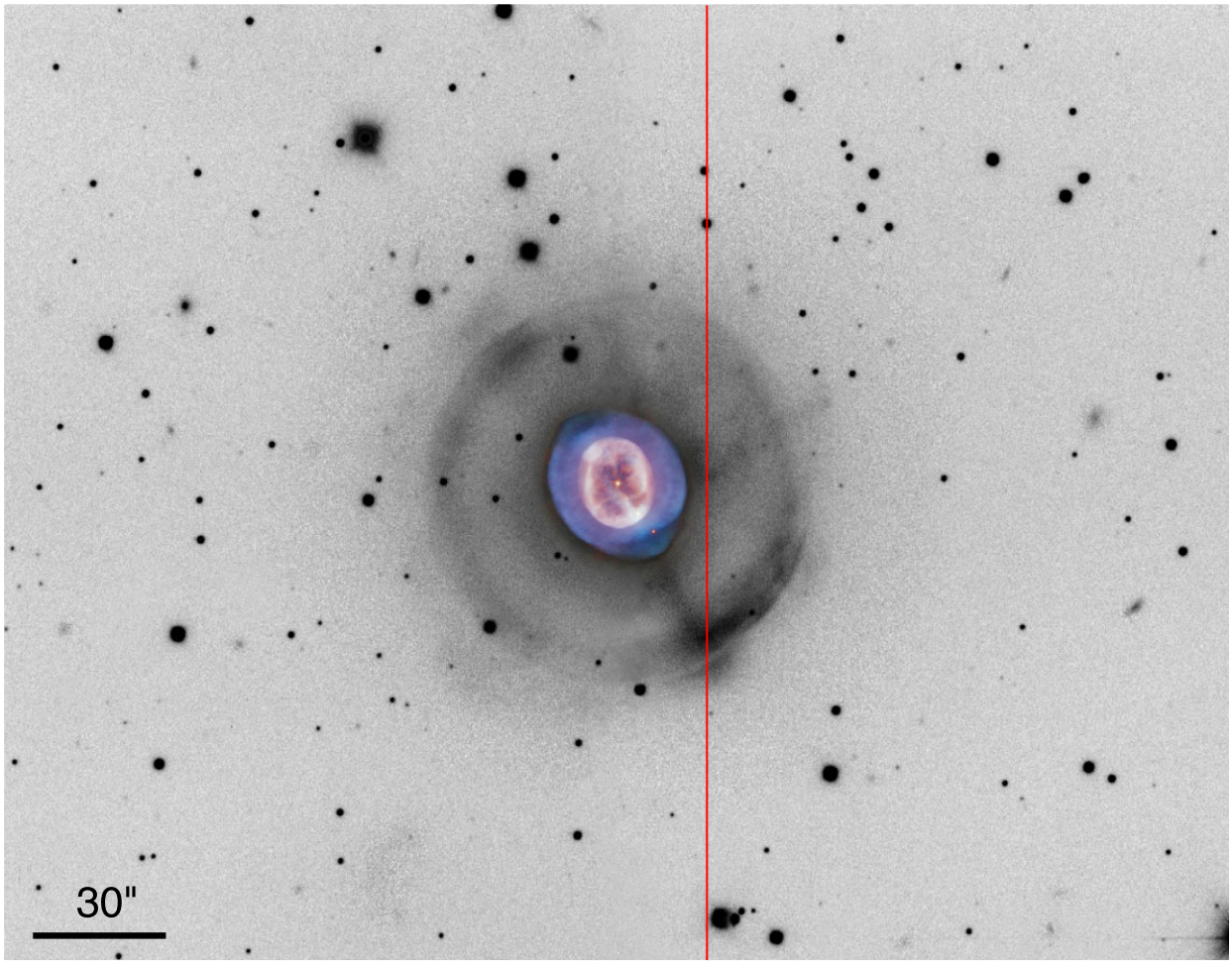

Figure 2. Composite INT WFC and NOT ALFOSC (greyscale) and *HST* ACS/WFC (colour) pictures of NGC 2022 accentuating the structure and extent of the nebular halo. The red solid line marks the position of the KPNO slit along the NS direction, offset 20 arcsec west from the CSPN. North is top, east to the left.

Table 1. Journal of high-dispersion spectroscopic observations of NGC 2022.

Telescope	Instrument	Slit	Filter	PA (°)	Binning	Date	Exp. time (s)	Seeing (arcsec)
SPM 2.1-m	MES	S1, major axis	Hα	35	2 × 2	2022 Apr 3	1800	1.6
			[O III]	35	2 × 2	2022 Apr 3	1800	1.6
		S2, minor axis	Hα	−55	2 × 2	2022 Apr 3	1800	1.6
			[O III]	−55	2 × 2	2022 Apr 3	1800	1.6
		S3, NS	Hα	0	4 × 4	2022 Oct 24	300	2.0
			[O III]	0	4 × 4	2022 Oct 24	300	2.0
		S4, EW	Hα	90	4 × 4	2022 Oct 24	300	2.0
			[O III]	90	4 × 4	2022 Oct 24	300	2.0
KPNO 4-m	Echelle	Major axis	[O III]	37	2 × 2	1984 Mar 25	1500	1.7
		NS; 20 arcsec W of CSPN	[O III]	0	2 × 2	1987 Sep 2	3000	2.4

respectively, and 9.3 ± 0.3 km s^{-1} for the KPNO echelle observations.

3 ANALYSES OF NEBULAR PROPERTIES

An inspection of the images of NGC 2022 in Figs 1 and 2 confirms its triple-shell structure reported by CJA87: a bright inner shell surrounded by a fainter envelope, and a large low-surface brightness halo, as accentuated in Fig. 2. All three components will be separately discussed in the analyses of morphology, kinematics, physical structure, and abundances presented in this section.

3.1 Morphology

The most detailed view of NGC 2022's bright inner shell and envelope is provided by the *HST* ACS/WFC images, although these

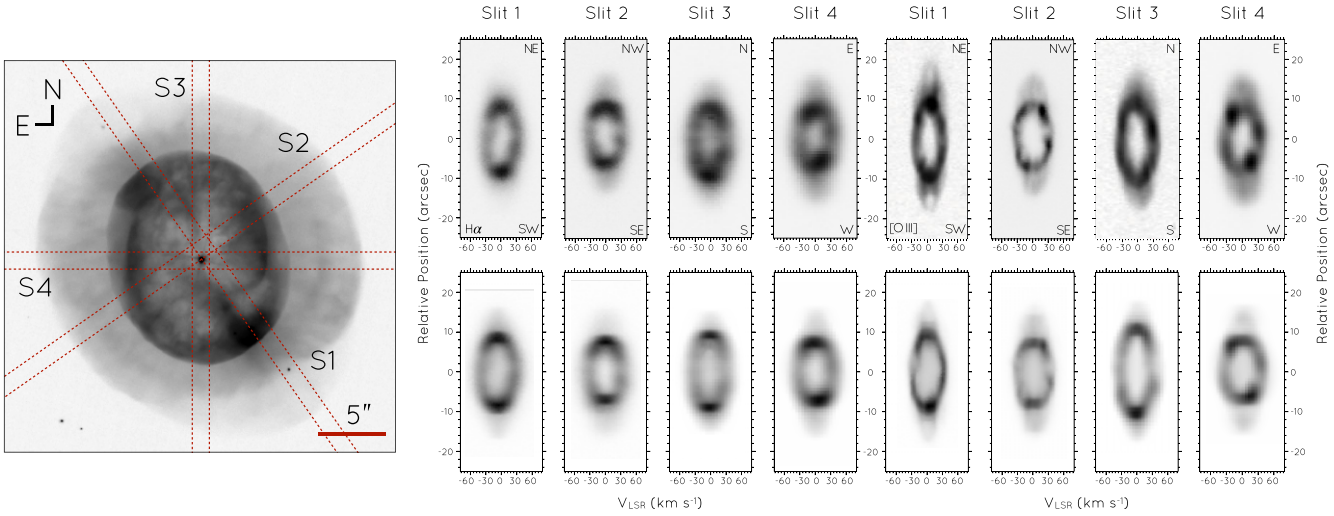

Figure 3. (Left) *HST* ACS/WFC *F*555*W* image of NGC 2022 with slit positions overlaid. (Right-Top Row) SPM MES position-velocity (PV) diagrams of NGC 2022 along four different position angles in the Hα (left half) and [O III] (Right half) emission lines, except the [O III] line of Slit 1, which is replaced by the KPNO 4-m echelle observation. (Right-Bottom Row) SHAPE synthetic PV diagrams for the corresponding slit positions and nebular lines.

were obtained through the broad-band *F*555*W* and *F*814*W* filters. The *F*555*W* image of NGC 2022 is dominated by the [O III] $\lambda\lambda$4959, 5007 emission lines, with <15 per cent contributions from He II λ4686 and Hβ, whereas NGC 2022 has no prominent emission lines in the band-pass of the *F*814*W* filter (Tsamis et al. 2003, also Section 3.3 in this paper). The *HST* colour-composite picture, shown in the top-left-hand panel of Fig. 1, thus depicts mainly the [O III] surface brightness variations of the nebula. It shows a double-shell structure, with a bright elliptical inner shell 21.4 × 16.7 arcsec in size and a fainter envelope. The bright inner shell of NGC 2022 is relatively thick, as compared with the crisp thin shell of NGC 6543, the Cat's Eye Nebula (Balick 2004). It has two bright knots on the NE and SW rims, and exhibits a notable set of filaments: two broad filaments appear to point towards the CSPN, and several finer filaments appear to be somewhat parallel to the minor axis. The envelope can be generally described as being rounder and smoother, with an angular size of 32 arcsec. The envelope itself shows a small break in its surface brightness near its radial mid-point, giving it a subtle 'double-layer' appearance. The envelope also shows two faint extensions, or ansae, along the NE-SW direction out to a radius of 18 arcsec. Interestingly, these ansae are well aligned with the two bright knots in the inner shell, but they are not with its major axis, which differs by ≈20° in position angle (PA).

The NOT ALFOSC [O III] and Hα images in the bottom panels of Fig. 1 basically confirm the morphological description provided by the *HST* ACS/WFC *F*555*W* and *F*814*W* images. The inner shell is not elliptical, but it rather has an ovel shape flattened at its poles. The bright knots, which are notable in the [O III] image, are indeed found to be aligned with the envelope's ansae. The [O III] emission of the envelope is highly structured, which is also shown in the *HST* *F*555*W* image (blue in Fig. 1 top-left), unlike the smooth envelope displayed in the Hα image. The radial variation of the envelope's [O III] surface brightness is confirmed to plateau half way through the envelope and then decline swiftly.

The faint large halo is detected both in the NOT ALFOSC [O III] and Hα images, being brighter and richer in small-scale structures in [O III]. The halo is best seen in Fig. 2, where its emission is mostly based on the deep INT WFC [O III] image presented by Corradi et al. (2003). The halo is limb-brightened (more clearly in [O III] than in Hα) and mostly round, with an average radius ≈43 arcsec. It shows a noticeable bright arc in the SW quadrant and a relatively bright spot in the NE quadrant. It also shows radial features, of which only the brightest along PA ≈200° appears to align with the CSPN, whereas those along PA ≈20° and 300° do not. Faint diffuse emission is found to extend beyond this round halo; however, the imperfect flat fielding of the NOT [O III] image makes it impossible to search for more extended features. We have thus examined carefully the OAJ JAST80 T80Cam *g*-SDSS images that have an excellent flat background. We are able to verify the halo morphology, extent, and features described above, and a small patch of emission at ≈2 arcmin SE from the CSPN, but do not see another extended halo. An analysis of the spatial extent of the low SB emission around NGC 2022 using the advanced Gnuastro techniques (Akhlaghi & Ichikawa 2015; Akhlaghi 2019) was, however, hampered by the extended wings of the instrumental PSF (Infante-Sainz, Trujillo & Román 2020).

3.2 Kinematics and physical structure

The SPM 2.1-m MES Hα and [O III] λ5007 and KPNO 4-m long-slit echelle [O III] λ5007 observations along the CSPN were used to produce the echellograms, i.e. position-velocity (PV) maps, shown in Fig. 3. The location and orientation of the slits are marked on an image in the left-hand panel of this figure. These PV maps provide kinematic information for the inner shell and envelope of NGC 2022. The faint outer halo is not detected in the SPM 2.1-m MES observations, but it is detected in the deep KPNO 4-m [O III] observation of a NS-oriented slit offset to 20 arcsec west of the CSPN (see Fig. 2).

The pattern of line splitting in the PV maps is characteristic for an expanding shell. It can be seen that the inner shell is brighter and expands faster than the outer envelope. Assuming that the expansion is symmetric about the central star, the average of the two velocity components at the central star represents the systemic velocity of the nebula. Using observations of the four slit positions passing through the CSPN, we derived a mean systemic velocity of $V_{\rm LSR} = 6 \pm 1\,{\rm km\,s^{-1}}$ and a projected radial expansion velocity of $V_{\rm exp} \sim 40\,{\rm km\,s^{-1}}$ at the centre. The knotty and filamentary structure of the inner shell is also clearly revealed in these PV maps. The overall

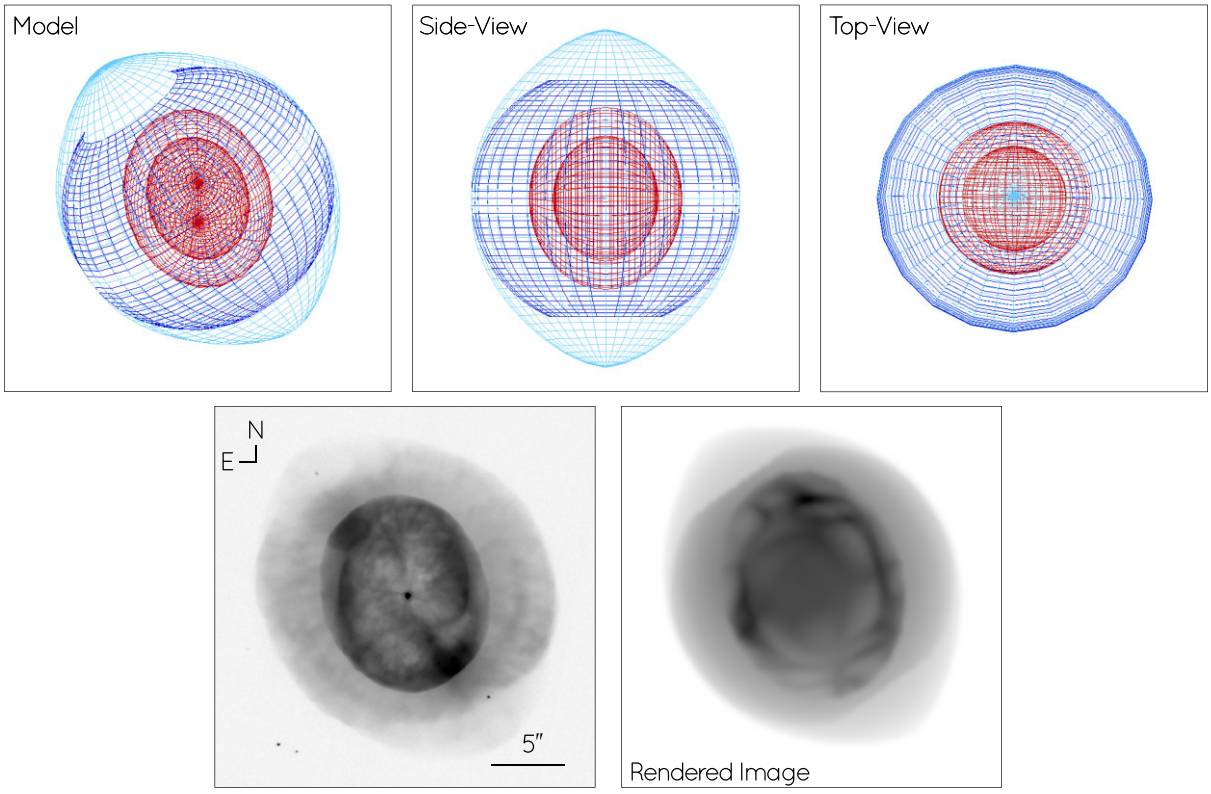

Figure 4. (top) SHAPE model of NGC 2022 along different lines of sight and (bottom) direct and rendered image.

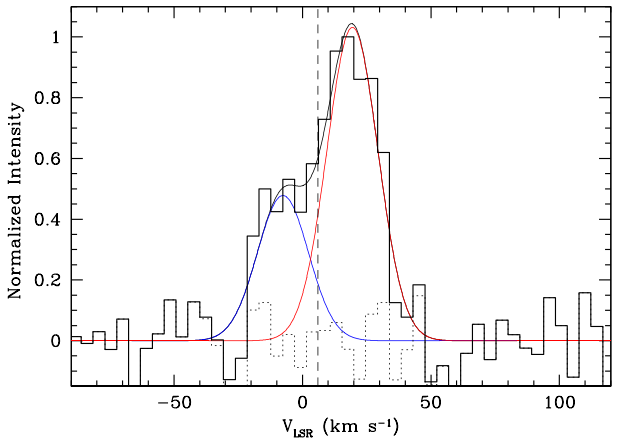

Figure 5. KPNO 4-m echelle velocity profile of the [O III] emission line in the halo of NGC 2022 extracted from a NS long-slit offset 20 arcsec west of its CSPN (solid histogram). The nebular systemic velocity is marked by a vertical dashed line. The profile is fitted with two Gaussian profiles (thin black lines) denoted each by thin blue and red lines. The fit residuals are shown by a dotted histogram.

shape of the spectral line of the inner shell is oval, yet there is notable brightening corresponding to filaments and knots as well as deviations from a regular expansion, seen particularly in the [O III] emission line, whose thermal width is smaller.

The spatio-kinematic modelling tool SHAPE (Steffen et al. 2011) was used to obtain synthetic PV maps and narrow-band images to be compared with the observed ones (Figs 3 and 4). For the inner shell, a tilted ellipsoidal shell was adopted, whereas the outer shell (the envelope) was modelled using an oval shell with a round inner cavity. The best-fit model of the inner shell has its major axis inclined from the sky plane by $10^\circ \pm 3^\circ$ and a major-to-minor axial ratio of $\simeq$1.3, which is very similar to the observed one given the small inclination of its major axis. The SHAPE model implies an expansion velocity of 43 ± 3 km s^{-1} along the major axis of inner shell, whereas the expansion velocity along the minor axis is 34 ± 3 km s^{-1}. The kinematical age of the inner shell, as determined from the SHAPE model, is 3200 ± 400 yr.

The outer envelope is only partially registered by the PV maps, as it is outshined by the bright emission of the inner shell. The velocity profiles of the envelope are resolved by the instrument, but do not show line splitting, except in the direction along the major axis at the location of the ansae. At the ansae (in slit 1), the PV map exhibits loop-like structures outside the expanding ring structure from the inner shell. The two resolved components at the ansae are split by $\simeq$26 km s^{-1}. Along other PAs, the outer envelope shows just broad velocity profiles; the intrinsic (instrumental width corrected) velocity profile at the innermost position of the envelope has FWHM $\approx$29 km s^{-1}. The velocity profile width of the envelope decreases with radius, as typically seen in envelopes of PNe (Guerrero, Villaver & Manchado 1998), which can be interpreted as resulting from the expansion of a filled shell. The observed PV maps are well-fitted by our SHAPE model, adopting the expansion velocity of 13 km s^{-1} derived from the two components detected along the major axis. Accordingly the kinematical age of the envelope derived from the SHAPE model is $\approx$15 000 yr.

The halo is only detected in the additional KPNO 4-m echelle deep (3000 s) observation of the [O III] line obtained with a slit oriented NS and offset by 20 arcsec to the west of the CSPN (as overlaid in Fig. 2). The halo is detected with a low signal-to-noise

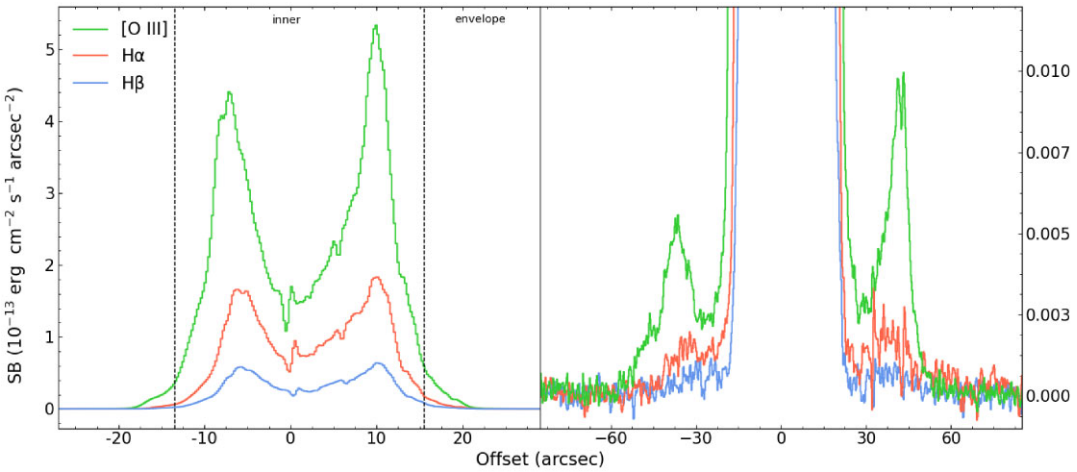

Figure 6. Hβ (blue), Hα (red), and [O III] λ5007 (green) surface brightness profiles extracted from the NOT ALFOSC spectrum of NGC 2022 along its major axis. The left-hand panel displays the full intensity range, whereas the right-hand panel zooms in into the halo emission, which is 100 to 500 times fainter than the main nebula. The vertical dashed lines mark the location of the inner shell and the envelope. North-east is to the left, south-west to the right.

Table 2. List of references where transition probabilities and collision strengths were taken to calculate ionic abundances.

Ions	Transition probabilities	Collision strengths
[O II]	Zeippen (1982)	Kisielius et al. (2009)
[O III]	Froese Fischer & Tachiev (2004)	Storey, Sochi & Badnell (2014)
[N II]	Froese Fischer & Tachiev (2004)	Tayal (2011)
[Ne II]	Galavis, Mendoza & Zeippen (1997)	McLaughlin & Bell (2000)
[Ne III]	Godefroid & Fischer (1984)	Giles (1981)
[Ne IV]	Galavis et al. (1997)	Dance et al. (2013)
[Ar IV]	Rynkun, Gaigalas & Jönsson (2019)	Ramsbottom, Bell & Keenan (1997)
[S II]	Rynkun et al. (2019)	Tayal & Zatsarinny (2010)

ratio, but a linesplit of $\simeq$27 km s^{-1} is clearly visible (see Fig. 5). After accounting for geometrical projections, this linesplit implies an expansion velocity of 15.5 $\pm$ 2.0 km s^{-1}, i.e. just slightly larger than the expansion velocity of the envelope, but smaller than that of the inner shell. The kinematical age of the halo, after accounting for the expansion velocity, distance, and angular size uncertainties, would be 31 000 $\pm$ 6000 yrs.

We note that the kinematical ages derived above may differ notably from the true nebular ages due to dynamical effects. Schönberner et al. (2014), based on results obtained by Jacob, Schönberner & Steffen (2013), present corrections factors for the ages of inner shells and envelopes, which imply true ages $\simeq$1.9 $\pm$ 0.5 times larger for inner shells and $\simeq$1.3 $\pm$ 0.3 for envelopes. Even more dramatic effects are expected to occur in PN haloes, with correction factors up to $\simeq$10 (Villaver, García-Segura & Manchado 2002). Therefore the true ages would be $\approx$6000 yrs for the inner shell, $\approx$20000 yrs for the envelope, and $\gg$31 000 yrs for halo.

3.3 Physical conditions and chemical abundances

One-dimensional (1D) optical spectra have been extracted to investigate the spectral properties, physical conditions, and chemical abundances of the inner shell, the outer envelope, the halo, and the central star. The apertures used to extract these 1D spectra are marked on the NOT ALFOSC Hα image of NGC 2022 (Fig. 1, bottom-left-hand panel), where aperture #1 with spatial extent 3.2 arcsec samples the region near the CSPN, apertures #2 and #2 arcmin with sizes 8.0 and 8.3 arcsec the inner shell, apertures #3 and #3 arcmin with sizes 7.7 and 7.3 arcsec the envelope, and apertures #4 and #4 arcmin with sizes 18.3 and 22.9 arcsec the halo. The spectra are shown in Appendix A Fig. A1.

The halo of NGC 2022 is much fainter than the inner shell and outer envelope, with an inner shell [O III] surface brightness (SB) peak $\approx$500 times higher than that of the halo (Fig. 6). The subtraction of the sky background may thus affect particularly the measurements of the line intensities in the faint halo, but special care was taken for this reduction step. The spatial extent and morphology of the halo SB profile (Fig. 6-*right*) agree with the deep image presented in Fig. 2: towards the SW, the halo emission peaks at $\simeq$42 arcsec and extends up to 50 arcsec, whereas towards the NE it peaks at $\simeq$37 arcsec with a noticeable shoulder up to 55 arcsec.

The IUE UV spectra have been used to determine the intensities of emission lines in the UV range from 1150 to 3000 Å. The LWP04612LL, LWP04621LL, LWP07428LL, and LWP17502LL spectra in the long wavelength range were averaged to improve the signal-to-noise ratio, while only the SWP08676LL spectrum in the short wavelength range was used because the inclusion of any other spectrum degraded its signal-to-noise ratio.

Lines in the spectra were then manually identified and measured by fitting Gaussian profiles using the standard IRAF *splot* task.

3.3.1 *Extinction and physical properties*

The spectral resolution of the NOT ALFOSC grism #7 used here is not sufficient to resolve the emission of the Pickering He II λ4860 line from that of Hβ or the Pickering He II λ6560 line from Hα. The intensities of these Pickering lines and thus their contributions to the Balmer lines are estimated from their theoretical ratios to the He II λ4686 line, although they depend on the physical conditions of the gas, which cannot be determined until the emission lines are corrected for extinction. Since the extinction determination itself relies on the ratio of the H I Balmer lines, an iterative process using the software PYNEB (Luridiana, Morisset & Shaw 2015) has been applied to derive simultaneously the logarithmic extinction coefficient c(Hβ) and physical conditions, i.e. electron temperature T_e and density n_e, accounting for the contribution of the He II Pickering lines to the H I Balmer lines.

Table 3. De-reddened emission lines fluxes from the NGC 2022 optical spectra. The intensities are normalized to the Hβ = 100.

	Near star		Inner shell		Envelope		Halo	
[O II] 3726 + 3729	3727.45	6.89 ± 0.61	3727.39	12.03 ± 0.12	3727.47	8.62 ± 0.97	0.00	...
H13 3734	0.00	...	3735.67	1.94 ± 0.08	0.00	...	0.00	...
H12 3750	0.00	...	3751.75	4.97 ± 0.10	0.00	...	0.00	...
[Fe VII] 3758	0.00	...	3759.23	6.96 ± 0.09	0.00	...	0.00	...
H11 3770	0.00	...	3771.78	5.34 ± 0.09	0.00	...	0.00	...
Fe V[?] 3783	0.00	...	3781.73	1.39 ± 0.13	0.00	...	0.00	...
H10 3797	3798.73	3.28 ± 0.42	3798.61	6.30 ± 0.08	3798.20	5.10 ± 0.72	0.00	...
He II 3813	3812.34	15.20 ± 0.48	3813.43	1.22 ± 0.10	0.00	...	0.00	...
He II 3833	3834.78	13.41 ± 0.48	3834.05	9.11 ± 0.08	3834.43	8.72 ± 0.81	0.00	...
[Ne III] 3868	3869.44	45.59 ± 0.50	3869.44	57.31 ± 0.08	3869.36	76.50 ± 0.77	0.00	...
Hζ 3889	3889.65	11.97 ± 0.45	3889.50	13.64 ± 0.08	3889.38	12.36 ± 0.76	0.00	...
He II 3923	0.00	...	3923.60	1.03 ± 0.09	0.00	...	0.00	...
Hϵ 3970	3969.14	25.85 ± 0.51	3969.14	35.07 ± 0.09	3969.79	38.18 ± 0.82	0.00	...
He I 4026	4025.42	3.44 ± 0.55	4026.04	1.70 ± 0.03	0.00	...	0.00	...
[S II] 4068	0.00	...	4069.52	2.64 ± 0.03	0.00	...	0.00	...
Hδ 4101	4102.01	22.34 ± 0.46	4101.92	29.58 ± 0.03	4101.84	26.68 ± 0.18	0.00	...
He II [a] 4200	0.00	...	4200.12	2.25 ± 0.03	4200.41	2.45 ± 0.18	0.00	...
[Fe V] 4227	0.00	...	4227.87	0.51 ± 0.03	4228.47	1.53 ± 0.20	0.00	...
C II 4267	4266.64	2.57 ± 0.52	4267.36	1.09 ± 0.03	4265.89	1.73 ± 0.22	0.00	...
Hγ 4340	4340.72	44.66 ± 0.50	4340.74	48.57 ± 0.03	4340.60	45.33 ± 0.18	4339.07	73.34 ± 8.41
[O III] 4363	4363.60	15.28 ± 0.51	4363.59	14.59 ± 0.03	4363.60	21.96 ± 0.17	0.00	...
N III 4379	4379.47	3.30 ± 0.63	4379.04	0.71 ± 0.03	0.00	...	0.00	...
[Fe II] 4452	0.00	...	4453.16	0.45 ± 0.04	0.00	...	0.00	...
He I 4471	0.00	...	4472.19	0.81 ± 0.03	4472.01	1.54 ± 0.19	0.00	...
He II 4543	4542.23	4.54 ± 0.45	4542.00	4.23 ± 0.01	4542.00	3.32 ± 0.11	0.00	...
N IV + O II 4608 + 4610	0.00	...	4608.15	0.24 ± 0.02	0.00	...	0.00	...
N III 4633	0.00	...	4633.72	1.11 ± 0.01	0.00	...	0.00	...
N III 4641	0.00	...	4641.36	2.04 ± 0.01	0.00	...	0.00	...
[S II] + O II 4648 + 4650	0.00	...	4649.61	1.61 ± 0.01	0.00	...	0.00	...
[Fe III]:C III:C IV 4658	0.00	...	4659.20	1.38 ± 0.01	0.00	...	0.00	...
He II 4686	4686.23	121.18 ± 0.67	4686.26	112.90 ± 0.02	4686.14	96.15 ± 0.17	4686.62	50.49 ± 6.43
[Ar IV] 4711	4710.15	18.95 ± 0.46	4710.07	16.18 ± 0.01	4710.93	17.13 ± 0.12	4710.16	57.24 ± 8.70
[Ne IV] 4724	4725.43	3.52 ± 0.46	4725.25	2.19 ± 0.01	4724.66	2.98 ± 0.16	0.00	...
[Ar IV] 4740	4740.79	14.25 ± 0.45	4740.65	12.53 ± 0.01	4740.56	12.56 ± 0.12	0.00	...
Hβ 4861	4861.77	100.00 ± 0.61	4861.82	100.00 ± 0.02	4861.71	100.00 ± 0.17	4861.08	100.00 ± 8.52
He I 4921	0.00	...	4921.26	0.55 ± 0.02	0.00	...	0.00	...
[O III] 4931	0.00	...	4931.65	1.41 ± 0.03	0.00	...	0.00	...
[O III] 4959	4959.47	207.01 ± 0.99	4959.52	250.49 ± 0.04	4959.44	404.19 ± 0.51	4959.43	296.90 ± 18.72
[O III] 5007	5007.44	630.28 ± 2.74	5007.47	765.39 ± 0.11	5007.37	1187.62 ± 1.45	5007.29	865.86 ± 52.45
? 5120	0.00	...	5120.52	0.40 ± 0.04	0.00	...	0.00	...
?[l] 5132	0.00	...	5132.25	0.28 ± 0.04	0.00	...	0.00	...
[Fe VI] 5145	5146.02	1.20 ± 0.63	5146.29	0.57 ± 0.05	0.00	...	0.00	...
[Fe VII] 5158	0.00	...	5159.87	0.28 ± 0.06	0.00	...	0.00	...
[Fe VI] 5176	0.00	...	5177.33	0.28 ± 0.01	0.00	...	0.00	...
? 5191	0.00	...	5191.89	0.18 ± 0.01	0.00	...	0.00	...
Fe II 5276	0.00	...	5277.48	0.11 ± 0.01	0.00	...	0.00	...
[Ca V] 5309	0.00	...	5308.54	0.28 ± 0.01	0.00	...	0.00	...
?[l] 5322	0.00	...	5322.76	0.14 ± 0.01	0.00	...	0.00	...
[Fe VI] 5335	0.00	...	5335.52	0.21 ± 0.01	0.00	...	0.00	...
?[l] 5346	0.00	...	5346.12	0.26 ± 0.01	0.00	...	0.00	...
He II 5411	5411.94	9.76 ± 0.24	5412.00	10.12 ± 0.01	5411.95	8.29 ± 0.09	0.00	...
[Fe VI] 5426	0.00	...	5426.79	0.19 ± 0.01	0.00	...	0.00	...
?[h] 5470	0.00	...	5470.55	0.11 ± 0.01	0.00	...	0.00	...
Fe VI[?] 5484	0.00	...	5485.31	0.09 ± 0.01	0.00	...	0.00	...
[Cl III] 5517	0.00	...	5518.12	0.64 ± 0.01	5518.53	0.79 ± 0.10	0.00	...
[Cl III] 5537	0.00	...	5538.22	0.52 ± 0.01	5537.60	0.63 ± 0.09	0.00	...
? 5592	0.00	...	5592.52	0.37 ± 0.01	5592.77	0.49 ± 0.08	0.00	...
Fe VI[?] 5631	0.00	...	5630.58	0.14 ± 0.01	0.00	...	0.00	...
[Fe VI] 5677	0.00	...	5677.66	0.20 ± 0.01	0.00	...	0.00	...
?[h] 5721	0.00	...	5721.27	0.14 ± 0.01	0.00	...	0.00	...
[N II] 5755	0.00	...	5755.55	0.09 ± 0.01	0.00	...	0.00	...
C IV 5801	0.00	...	5801.48	0.49 ± 0.01	0.00	...	0.00	...
C IV 5811	0.00	...	5812.22	0.31 ± 0.01	0.00	...	0.00	...
He I 5876	5875.22	5.08 ± 0.37	5875.82	2.52 ± 0.01	0.00	...	0.00	...

Table 3 – *continued*

	Near star		Inner shell		Envelope		Halo	
Fe II[?] 5913	0.00	...	5913.79	0.14 ± 0.01	0.00	...	0.00	...
He II 5931	0.00	...	5932.20	0.17 ± 0.01	0.00	...	0.00	...
He II[a] 5953	0.00	...	5953.27	0.18 ± 0.01	0.00	...	0.00	...
He II[a] 5977	0.00	...	5977.23	0.17 ± 0.01	0.00	...	0.00	...
Fe III[?] 6004	0.00	...	6004.66	0.25 ± 0.00	0.00	...	0.00	...
He II[a] 6036	0.00	...	6036.79	0.26 ± 0.00	0.00	...	0.00	...
He II[a] 6074	0.00	...	6074.04	0.27 ± 0.00	0.00	...	0.00	...
Ca V[?] 6086	6086.38	0.69 ± 0.21	6086.36	0.22 ± 0.00	0.00	...	0.00	...
[Kr IV] 6101	6101.23	0.67 ± 0.23	6101.77	0.72 ± 0.00	0.00	...	0.00	...
He II[a] 6118	6119.05	0.51 ± 0.19	6118.26	0.31 ± 0.00	0.00	...	0.00	...
He II[a] 6170	0.00	...	6170.74	0.32 ± 0.00	0.00	...	0.00	...
He II[a] 6234	0.00	...	6234.07	0.37 ± 0.00	0.00	...	0.00	...
[S III] 6312	6311.41	1.40 ± 0.23	6311.70	2.23 ± 0.00	6311.43	2.25 ± 0.10	0.00	...
?[h] 6326	0.00	...	6327.00	0.13 ± 0.00	0.00	...	0.00	...
He II[a] 6406	6405.83	1.03 ± 0.28	6406.34	0.62 ± 0.00	0.00	...	0.00	...
[Ar V] 6435	6434.72	2.74 ± 0.22	6434.83	1.91 ± 0.00	6434.66	1.29 ± 0.09	0.00	...
?[l] 6500	6500.21	1.58 ± 0.23	6500.33	1.21 ± 0.01	0.00	...	0.00	...
He II 6526	6526.65	0.69 ± 0.13	6526.87	1.09 ± 0.01	0.00	...	0.00	...
[N II] 6548	6549.18	0.76 ± 0.20	6548.51	1.12 ± 0.01	6546.29	1.38 ± 0.07	0.00	...
Hα 6563	6562.48	277.29 ± 1.20	6562.54	278.63 ± 0.04	6562.46	279.20 ± 0.34	6563.92	279.20 ± 17.15
[N II] 6584	6583.17	2.25 ± 0.09	6583.21	3.32 ± 0.01	6583.31	4.29 ± 0.05	6585.90	24.20 ± 3.34
He I 6678	6679.82	1.92 ± 0.12	6679.91	1.48 ± 0.01	6679.87	2.15 ± 0.07	0.00	...
[S II] 6717	6716.95	0.59 ± 0.09	6716.38	0.83 ± 0.01	6717.30	0.95 ± 0.05	0.00	...
[S II] 6731	6730.90	0.61 ± 0.07	6730.66	0.98 ± 0.01	6731.32	0.79 ± 0.04	0.00	...
He II 6890	6890.71	0.67 ± 0.07	6890.61	0.78 ± 0.01	0.00	...	0.00	...
[Ar V] 7005	7005.47	4.38 ± 0.07	7005.29	3.34 ± 0.01	7005.31	1.77 ± 0.04	0.00	...
He I 7065	0.00	...	7063.94	0.47 ± 0.01	0.00	...	0.00	...
$\log_{10}$ F(Hα)	–	− 13.04		− 12.13	–	− 13.32	–	−14.67 ± 0.02

Notes.[a] Ion identification adopted from Tsamis et al. (2003).
[l] Unidentified low-excitation ion.
[h] Unidentified high-excitation ion.

The Hα to Hβ line intensity ratios (He II Pickering lines corrected) are compared with the expected ratios from the Case B recombination models to determine c(Hβ). The extinction is found to be consistent among the different morphological components, with an average c(Hβ) of 0.06 ± 0.01. A list of all the observed dereddened line intensities normalized to Hβ = 100 is given in Table 3.

We note that the UV spectra were obtained from a 10 × 23 arcsec aperture centred at the location of the CSPN and thus covered the inner shell and part of the envelope. Since the inner shell emission dominates that of the envelope, as illustrated by their total Hα fluxes (bottom row of Table 3) and SB profile (Fig. 6), it is thus assumed that the line intensities measured in the *IUE* UV spectra correspond to those of the inner shell. Once the emission lines from the spectra were dereddened with the extinction derived above, an aperture correction should be applied to the UV line intensities. This correction was made by assuming a theoretical ratio for the He II λ1640/λ4686 line ratio at the same T_e and n_e as for extinction. The emission line intensities, normalized to Hβ = 100, are given in Table 4.

The 1D spectra of the central star and, very notably, the bright inner shell (Fig. A1) present a wealth of emission lines whose identification, particularly for the faintest ones, is hampered by the coarse spectral resolution. The line list derived from echelle observations provided by Tsamis et al. (2003) has guided us to identify the lines marked by an 'a' superscript in Table 3. Still, the depths of the spectra presented here exceed those presented by Tsamis et al. (2003), and a number of emission lines lacked clear identifications. These are marked in Table 3 with the superscripts 'l' and 'h' to denote lines whose spatial distributions imply low- and high-excitation ions, respectively.

Table 4. De-reddened emission lines fluxes from the NGC 2022 uv spectra. The intensities are normalized to the Hβ = 100.

Ions	λ_{obs}	I(λ)
? 1215	1215.28	314.53 ± 20.13
O IV] 1401	1401.53	154.15 ± 13.33
N IV] 1486	1485.39	92.16 ± 1.06
C IV 1549	1548.88	1308.23 ± 9.93
[Ne IV] 1601	1601.01	26.87 ± 6.27
He II 1640	1641.49	952.76 ± 7.28
O III] 1663	1661.82	32.04 ± 6.68
C III] 1750	1750.98	41.39 ± 6.75
N III] 1908	1908.61	868.26 ± 6.04
[Ne IV] 2423	2422.55	406.10 ± 5.07
He II 2511	2510.91	32.62 ± 2.13
He II 2733	2731.84	63.03 ± 1.73
? 2842	2842.20	46.75 ± 2.67
O III 3046	3045.41	24.11 ± 6.00
O III + [Ne II] 3130	3130.91	177.81 ± 1.71
He II 3201	3201.95	150.49 ± 1.84
F(Hβ_t)	–	-12.094 ± 0.001

The temperatures and densities derived from the different diagnostic line ratios are shown in Fig. 7 (no line diagnostics were available for the halo). The [S II] λλ6716, 6731, [Ar IV] λλ4711, 4740, and [Cl III] λλ5517, 5537 emission line doublets were used to determine the electron density (the latter only for the inner shell and envelope).

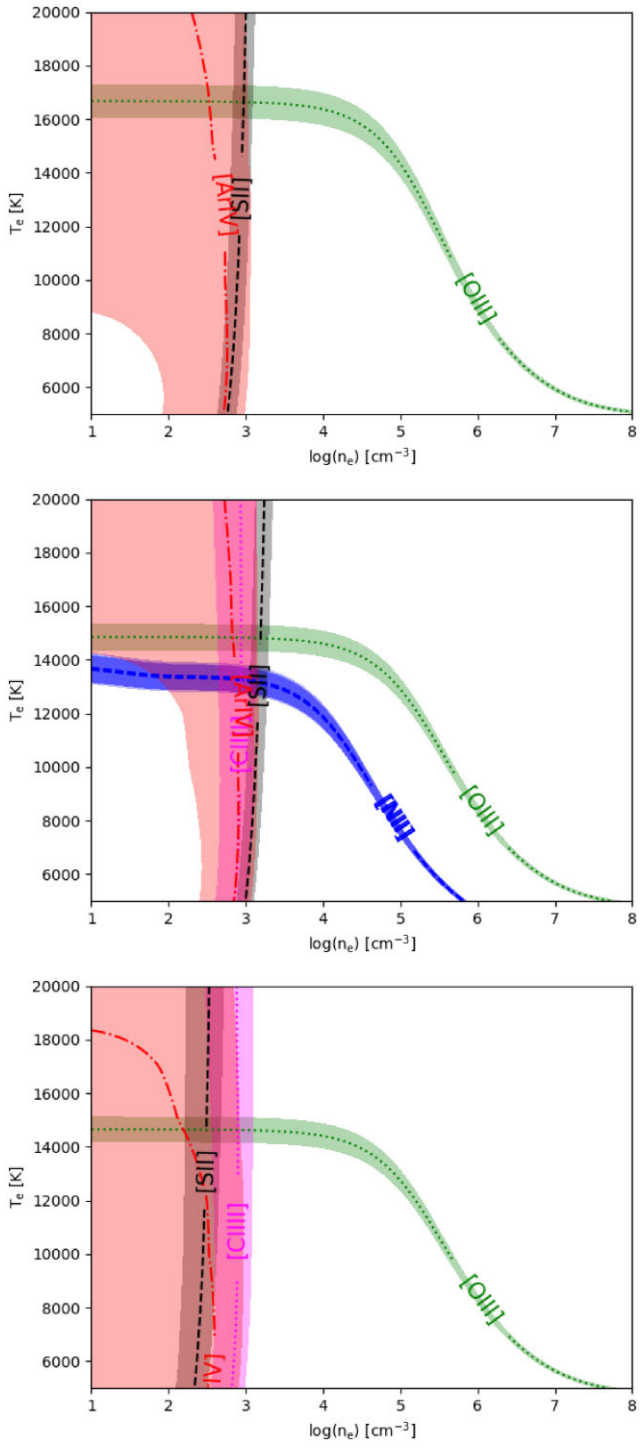

Figure 7. T_e versus n_e diagrams for the star (top), inner rim (middle), and outer evelope (bottom) regions of NGC 2022. The lines denote the temperature and density derived from observed line ratios, and the shadowed areas their 1σ uncertainties.

As for electron temperatures, the auroral [O III] λ4363 to nebular [O III] λλ4959, 5007 emission line ratio and the auroral [N II] λ5755 to nebular [N II] λλ6548, 6584 (only for the inner shell) emission line ratio were used. The electron density derived from the [S II] line doublet seems to decrease from the innermost regions, with $n_e \approx$ 1300 cm^{-3}, to the outer envelope, with $n_e \approx 500$ cm^{-3}. On the other hand, the electron temperature is higher, $T_e \approx 16\,500$ K, in the central region near the CSPN, and then decreases down to ≈14 500 K in the inner shell and envelope.

The values of T_e and n_e adopted for the abundance calculations in the following subsection correspond to the crossing points between the [O III] and [S II] diagnostic lines in these diagrams (Fig. 7). We remark that these same values were used to compute the He II Pickering lines contribution to Hβ and Hα and to determine the theoretical Hα to Hβ line ratio for the determination of the extinction.

3.3.2 *Chemical abundances*

Abundances relative to H were derived from collisionaly excited lines (CELs) for ionic species of O, N, Ne, Ar, S, and Cl and from recombination lines for He. The transition probabilities and collision strengths used to compute ionic abundances are listed in Table 2. The resultant ionic abundances are given in Tables 5 and 6.

The total He abundance for all regions was obtained by adding the ionic abundances of He^{++} derived from the He II λ4686 line and the average of the abundances of He^{+} derived from all available He I lines. As for the other elements, namely O, N, Ne, S, and Cl, the ionization corrections factors (ICFs) presented by Delgado-Inglada, Morisset & Stasińska (2014) and Kingsburgh & Barlow (1994) (hereinafter DM14 and KB94, respectively) were adopted to estimate the contributions of ions inaccessible from available spectra to the total abundances. These two sets of ICFs are specific for PNe and both are based on similar criteria to assess the likely ionization fractions using parameters derived from He I, He II, [O II], and [O III] emission line ratios. We note that the applicability of the ICFs proposed by DM14, which depend on the number of detected lines, is more restrictive than that of KB94. However, their final abundance estimations remain consistent with each other. In particular, DM14 defines the ionic fractions ν and ω that are used to validate different ICF selection (see table 3 in DM14), where

$$\omega = \frac{[\mathrm{O\,III}]}{[\mathrm{O\,II}] + [\mathrm{O\,III}]}, \qquad \nu = \frac{\mathrm{He\,II}}{\mathrm{He\,II} + \mathrm{He\,I}}. \tag{1}$$

The values of ν and ω are also given in Table 7. The total Ar abundances could not be calculated because of the lack of [Ar III] lines in the optical spectrum, and no ICF is available.

The *IUE* UV spectrum provides information on the line intensities of high-ionization species of N and O from the inner shell (Table 4) that has been used to derive ionic abundances of N^{++}, N^{3+}, and O^{3+} (Table 5). These have been used to derive the O and N abundances listed in Table 7 by the direct addition of all available ionic abundances. We notice that the abundances obtained this way are ≃1 dex higher than those derived using ICFs and ≃5 times higher than the Solar N and O abundances. Whereas these high abundances suggest that a significant fraction of N and O may be in high excitation species, the different aperture sizes of the spectra and uncertainties in extinction correction in the UV cast significant uncertainties in these results; thus, these high abundances will not be considered in the following discussion.

4 DISCUSSION AND CONCLUDING REMARKS

The analysis of the chemical abundances of NGC 2022 implies very similar abundances throughout the different nebular shells. The average He/H abundances of the inner shell and envelope are similar, 0.12, whereas the non-detection of the He I λ5876 emission line in the halo only allows the determination of a lower limit for the He abundances, which is within error limits consistent with those of the inner shell and envelope. The inner shell and envelope also have

Table 5. Ionic abundances from CELs.

X^i +/H^+	Lines	Near star	Inner shell	Envelope	Halo
O^+/H^+	λλ 3726, 3729	6.04 ± 0.04	6.50 ± 0.00	6.19 ± 0.05	...
O^{2+}/H^+	λλ 4959, 5007	7.73 ± 0.00	7.93 ± 0.00	8.14 ± 0.00	8.49 ± 0.02
O^{3+}/H^+	λ 1401	...	9.39 ± 0.04	...	...
N^+/H^+	λ 6584	5.20 ± 0.02	5.45 ± 0.00	5.58 ± 0.01	6.70 ± 0.06
N^{2+}/H^+	λ 1752	...	8.15 ± 0.07	...	...
N^{3+}/H^+	λ 1486	...	8.32 ± 0.01	...	...
Ne^{2+}/H^+	λλ 3868, 3967	6.98 ± 0.00	7.21 ± 0.00	7.35 ± 0.00	...
Ne^{3+}/H^+	λ 1601	...	8.52 ± 0.10	...	...
Ne^{3+}/H^+	λ 2423	...	8.46 ± 0.01	...	...
Ne^{3+}/H^+	λλ 4715, 4726	8.14 ± 0.06	8.21 ± 0.00	8.41 ± 0.02	...
Ar^{3+}/H^+	λλ 4711, 4740	6.06 ± 0.01	6.12 ± 0.00	6.15 ± 0.00	7.15 ± 0.07
S^+/H^+	λλ 6716, 6730	4.09 ± 0.04	4.39 ± 0.00	4.30 ± 0.01	...
S^{2+}/H^+	λ 6312	5.74 ± 0.07	6.08 ± 0.00	6.11 ± 0.02	...
Cl^{2+}/H^+	λλ 5517, 5537	...	4.43 ± 0.01	4.52 ± 0.04	...

Table 6. Ionic abundances from ORLs.

He^i +/H^+	Lines	Near star	Inner shell	Envelope	Halo
O^{2+}/H^+	λ 4650	...	9.86 ± 0.01	...	...
N^{3+}/H^+	λ 4641	...	8.72 ± 0.01	...	...
He^+/H^+	λ 4471	...	10.19 ± 0.01	10.49 ± 0.04	...
He^+/H^+	λ 5876	10.52 ± 0.01	10.20 ± 0.01	...	...
He^+/H^+	λ 6678	10.64 ± 0.01	10.52 ± 0.01	10.74 ± 0.04	...
He^{2+}/H^+	λ 1640	...	11.07 ± 0.01	...	...
He^{2+}/H^+	λ 4686	11.03 ± 0.01	10.99 ± 0.01	10.92 ± 0.04	10.61 ± 0.01

Table 7. Total abundances computed using ICFs listed in Delgado-Inglada et al. (2014) (DM14) and Kingsburgh & Barlow (1994) (KB94) and direct addition from ionic abundances, if possible. The values of the parameters ν and ω (see equation 1) define by Delgado-Inglada et al. (2014), are presented in the bottom. The uncertainties shown are those associated with the ICF adopted, if any.

X/H	ICF	Near star	Inner shell	Envelope	Halo
He/H	Direct addition	11.12 ± 0.01	11.08 ± 0.01	11.05 ± 0.04	≥10.61 ± 0.01
O/H	KB94	8.21	8.44	8.54	8.49
	DM14	8.30 ± 0.13	8.52 ± 0.12	8.59 ± 0.17	9.72 ± 0.03
	Direct addition	7.74	9.41	8.14	8.49
N/H	KB94	7.37	7.39	7.93	...
	DM14	7.31[a]	7.34[a]	7.85[a]	...
	Direct Addition	...	8.55	...	...
Ne/H	KB94	7.46	7.72	7.75	...
	DM14	$7.6^{+0.4}_{-0.6}$	$7.9^{+0.5}_{-0.7}$	$7.8^{+0.3}_{-0.5}$	...
	Direct addition	8.17	8.25	8.45	...
S/H	KB94	6.32	6.58	6.74	...
	DM14	$6.7^{+0.3}_{-0.6}$	$6.98^{+0.09}_{-0.21}$	$7.0^{+0.2}_{-0.5}$	...
Cl/H	DM14	...	$5.34^{+0.12}_{-0.21}$	$5.41^{+0.25}_{-0.45}$	...
ω	–	0.98	0.96	0.99	1.0
ν	–	0.81	0.82	0.74	1.0

Note.[a] If ω is greater than 0.95, it is not recommended to use this ICF because the uncertainties are very high.

similar O/H and N/H abundances, (2–4) × 10^{-4} for O/H and (2–9) × 10^{-5} for N/H. Once again, the halo's non-detection of key emission lines of [O II] makes it difficult to determine O and N abundances there, but its O/H determined using KB94 ICFs is consistent with those of the inner shell and envelope. Averaged values of 3 × 10^{-4} for O/H and 4 × 10^{-5} for N/H will be adopted, which are consistent within a factor of two with the average N/H and O/H abundances of the whole nebula of 1.0 × 10^{-4} and 4.7 × 10^{-4}, respectively, reported by Pottasch & Bernard-Salas (2010). Finally, the N/O ratio is also quite constant throughout the different nebular regions, all in the range of 0.07 to 0.25. An average value of 0.14 will be adopted.

The low values of the He/H abundances and N/O abundance ratio are consistent with a Type II classification (Peimbert 1978). The comparison with the theoretical predictions of the stellar yields of AGB stars of Karakas & Lugaro (2016) for subsolar progenitor is consistent with an initial mass of the progenitor $\leq$4 $M_\odot$.

The true age of the envelope $\simeq$20 000 yr derived from its kinematical age (see 3.2) is a reasonable approximation of the stellar evolutionary time scale, which is otherwise notably large. The relatively high effective temperature and low surface gravity ($T_{\rm eff}$ = 100 000 K, $\log g$ = 5.3, McCarthy et al. 1997) place the CSPN of NGC 2022 close to the knee of the evolutionary track of post-AGB stars, in agreement with the large true age of the envelope only for progenitor stars of low initial mass (e.g. Bloecker 1995; Miller Bertolami 2016).

The ionized mass of the inner shell and envelope can be derived from the volume of each shell and their measured electron densities as

$$M_{\rm shell} = \mu\, m_{\rm p}\, n_{\rm p} V f, \tag{2}$$

where μ is the mean molecular weight, which can be assumed to be 1.44 for the observed He/H ratio, $m_{\rm p}$ is the proton mass, $n_{\rm p}$ is the proton density, which can be expressed as 0.8 $\times$ $n_{\rm e}$, V is the volume occupied by the shell, and f is the filling factor. The volume of the inner shell and envelope derived from their angular sizes and distance to NGC 2022 are $\approx$1.5 $\times$ 10^{53} and $\approx$6.0 $\times$ 10^{53} cm^3, whereas their electron densities were computed in section 3.3.1, resulting in

$$M_{\rm in} = 0.19 \times f_{\rm in}\, M_\odot, \quad M_{\rm env} = 0.29 \times f_{\rm env}\, M_\odot. \tag{3}$$

The values of the filling factor f of each shell can be estimated from the intrinsic Hα fluxes (for instance, Pottasch 1984)

$$4\,\pi\, d^2\, F(\mathrm{H}\alpha) = 4\,\pi\, \epsilon(\mathrm{H}\alpha)\, V\, f\, n_{\rm e}\, n_{\rm p}, \tag{4}$$

where d is the distance and ϵ(Hα) is the Hα emission coefficient, which can be approximated by 2.0 $\times$ 10^{-26} erg cm^3 s^{-1} for the observed electron temperature of 14 500 K. The observed Hα fluxes, as derived from the NOT ALFOSC Hα image (Fig. 1 top-right) flux-calibrated using the Hα SB profile derived from the NOT ALFOSC spectrum (Fig. 1), are 4.1 $\times$ 10^{-11} erg cm^{-2} s^{-1} for the inner shell and 1.5 $\times$ 10^{-11} erg cm^{-2} s^{-1} for the envelope. These figures need to be increase by $\simeq$10 per cent to account for extinction in order to obtain the intrinsic Hα fluxes. Equation (4) thus implies $f_{\rm in}$ of 0.56 and $f_{\rm env}$ of 0.34 for total ionized masses of 0.11 $M_\odot$ for the inner shell and 0.10 $M_\odot$ for the envelope.

Finally, the ionized mass of the outer halo can be derived from the volume of this shell and its intrinsic Hα flux (Pottasch 1984)

$$M_{\rm shell} = \mu\, m_{\rm p} \sqrt{\frac{4\,\pi\, d^2 F(\mathrm{H}\alpha)\, V\, f}{4\,\pi\, \epsilon(\mathrm{H}\alpha)}}. \tag{5}$$

The intrinsic Hα flux of the halo can be estimated to be $\simeq$2 $\times$ 10^{-13} erg cm^{-2} s^{-1} from its Hα SB profile (Fig. 1), whereas a volume of 1.4 $\times$ 10^{55} cm^{-3} is derived from its angular size and distance. The halo mass is thus found to be 0.10 $\times$ $f_{\rm halo}^{1/2}$ $M_\odot$.

Adopting the CSPN mass of 0.64 $M_\odot$ reported by McCarthy et al. (1997), which is otherwise typical for CSPNe, the total mass of NGC 2022 amounts $\approx$0.9 $M_\odot$. The total ionized mass of the main nebula and its halo are very consistent with those expected for the final gasps of low-mass stars, in the range $\leq$1.5 $M_\odot$ (Vassiliadis & Wood 1993).

To sum up, the evolutionary time-scale of the CSPN of NGC 2022 and its total mass point to a low-mass $\leq$1.5 $M_\odot$ progenitor star, whereas the nebular chemical abundances can only constrain it to have a mass $\leq$4 $M_\odot$. If the mass of the progenitor star were in the higher range, then a significant amount of mass was left behind by the progenitor, whose radial (14.2 km s^{-1}) and tangential (16.8 km s^{-1}) velocities are not particularly high, but sufficient to travel $\approx$2.2 pc in a typical inter-pulse time-lapse of 10^5 yr. The radius of the present halo, $\simeq$0.44 pc, is within this distance, whereas the patch of diffuse emission $\approx$2 arcmin SE is $\approx$1.2 pc from the CSPN and might thus be attributed to a previous episode of mass lost.

ACKNOWLEDGEMENTS

BMM and MAG acknowledge financial support from grants CEX2021-001131-S funded by MCIN/AEI/10.13039/501100011033 and PGC2018-102184-B-100 from the Spanish Ministerio de Ciencia, Innovación y Universidades (MCIU). YHC acknowledges the research grant NSTC 111-2112-M-001-063 from the National Council of Science and Technology of Taiwan. JAT thanks support from the UNAM DGAPA PAPIIT number IA101622. GR-L acknowledge support from CONACYT (grant 263373).

This paper is based in part on ground-based observations from (1) the Observatorio Astronómico Nacional at the Sierra de San Pedro Mártir (OAN-SPM), which is a national facility operated by the Instituto de Astronomía of the Universidad Nacional Autónoma de México. We are grateful to the staff of OAN-SPM, specially to Tomás Verdugo González, support astronomer, and Marissa Botello Nava for their assistantship during observations. (2) ALFOSC at the NOT of the Observatorio de El Roque de los Muchachos (ORM), an instrument provided by the Instituto de Astrofísica de Andalucía (IAA) under a joint agreement with the University of Copenhagen and NOTSA, and (3) the JAST80 telescope and T80Cam camera for the J-PLUS project at the Observatorio Astrofísico de Javalambre (OAJ), in Teruel, owned, managed, and operated by the Centro de Estudios de Física del Cosmos de Aragón (CEFCA). We thank CEFCA for allocation of Director's Discretionary Time to this program. Funding for OAJ, JAST80, T80Cam, UPAD, and CEFCA has been provided by the Governments of Spain and Aragón through the Fondo de Inversiones de Teruel and their general budgets; the Spanish Ministry of Economy and Competitiveness (MINECO) under AYA2012-30789, and ICTS-2009-14; and European FEDER funding (FCDD10-4E-867, FCDD13-4E-2685). The Brazilian agencies FINEP, FAPESP, and the National Observatory of Brazil have also contributed to the OAJ funding. This research is also based on observations made with the NASA/ESA *HST* obtained from the Space Telescope Science Institute, which is operated by the Association of Universities for Research in Astronomy, Inc., under NASA contract NAS 5-26555. The observations used here are associated with program 11599. Data of the IUE satellite downloaded from the INES database were also used.

This work has made extensive use of NASA's Astrophysics Data System (ADS). We acknowledge the OAJ Data Processing and Archiving Unit (UPAD) for reducing and calibrating the OAJ data used in this work. This research made use of IRAF, distributed by the National Optical Astronomy Observatory, which is operated by the Association of Universities for Research in Astronomy (AURA) under a cooperative agreement with the National Science Foundation. This paper made also use of the software PyNeb and SHAPE.

In memoriam Prof. Jim Kaler.

DATA AVAILABILITY

The data underlying this work are available in the article. The data files will be shared on request to the first author.

REFERENCES

Akhlaghi M., 2019, preprint (arXiv:1909.11230)
Akhlaghi M., Ichikawa T., 2015, ApJS, 220, 1
Bailer-Jones C. A. L., Rybizki J., Fouesneau M., Demleitner M., Andrae R., 2021, AJ, 161, 147
Balick B., 1987, AJ, 94, 671
Balick B., 2004, AJ, 127, 2262
Bloecker T., 1995, A&A, 299, 755
Cenarro A. J. et al., 2014, Proc. SPIE, 9149, 91491I
Chu Y.-H., Jacoby G. H., Arendt R., 1987, ApJS, 64, 529
Chu Y.-H., Manchado A., Jacoby G. H., Kwitter K. B., 1991, ApJ, 376, 150
Corradi R. L. M., Schönberner D., Steffen M., Perinotto M., 2003, MNRAS, 340, 417
Dance M., Palay E., Nahar S. N., Pradhan A. K., 2013, MNRAS, 435, 1576
Delgado-Inglada G., Morisset C., Stasińska G., 2014, MNRAS, 440, 536
Froese Fischer C., Tachiev G., 2004, At. Data Nucl. Data Tables, 87, 1
Galavis M. E., Mendoza C., Zeippen C. J., 1997, A&AS, 123, 159
Giles K., 1981, MNRAS, 195, 63P
Godefroid M., Fischer C. F., 1984, J. Phys. B Atom. Mol. Phys., 17, 681
Guerrero M. A., Villaver E., Manchado A., 1998, ApJ, 507, 889
Infante-Sainz R., Trujillo I., Román J., 2020, MNRAS, 491, 5317
Jacob R., Schönberner D., Steffen M., 2013, A&A, 558, A78
Karakas A. I., Lugaro M., 2016, ApJ, 825, 26
Kingsburgh R. L., Barlow M. J., 1994, MNRAS, 271, 257
Kisielius R., Storey P. J., Ferland G. J., Keenan F. P., 2009, MNRAS, 397, 903
Luridiana V., Morisset C., Shaw R. A., 2015, A&A, 573, A42
Marin-Franch A., Taylor K., Cenarro J. et al., 2015, IAU General Assembly.
McCarthy J. K., Mendez R. H., Kudritzki R.-P., 1997, Planetary Nebulae, 180, 120
McLaughlin B. M., Bell K. L., 2000, J. Phys. B Atom. Mol. Phys., 33, 597
Meaburn J., López J. A., Gutiérrez L., Quiróz F., Murillo J. M., Valdéz J., Pedrayez M., 2003, RMxAA, 39, 185
Miller Bertolami M. M., 2016, A&A, 588, A25
Peimbert M., 1978, IAUS, 76, 215
Pottasch S. R., 1984, Astrophysics and Space Science Library, vol 107. Springer, Dordrecht, available at: https://doi.org/10.1007/978-94-009-7233-9_9
Pottasch S. R., Bernard-Salas J., 2010, A&A, 517, A95
Ramsbottom C. A., Bell K. L., Keenan F. P., 1997, MNRAS, 284, 754
Rynkun P., Gaigalas G., Jönsson P., 2019, A&A, 623, A155
Sabbadin F., Bianchini A., Hamzaoglu E., 1984, A&A, 136, 193
Schönberner D., Jacob R., Lehmann H., Hildebrandt G., Steffen M., Zwanzig A., Sandin C., Corradi R. L. M., 2014, Astron. Nachr., 335, 378
Steffen W., Koning N., Wenger S., Morisset C., Magnor M., 2011, IEEE Trans. Vis. Comput. Graphics, 17, 454
Storey P. J., Sochi T., Badnell N. R., 2014, MNRAS, 441, 3028
Tayal S. S., 2011, ApJS, 195, 12
Tayal S. S., Zatsarinny O., 2010, ApJS, 188, 32
Tody D., 1993, ASPC, 52, 173
Tsamis Y. G., Barlow M. J., Liu X.-W., Danziger I. J., Storey P. J., 2003, MNRAS, 345, 186
Vassiliadis E., Wood P. R., 1993, ApJ, 413, 641
Villaver E., García-Segura G., Manchado A., 2002, ApJ, 571, 880
Zeippen C. J., 1982, MNRAS, 198, 111

APPENDIX A: SPECTRA

The spectra extracted from the apertures showed in Fig. 1 are presented in Fig. A1

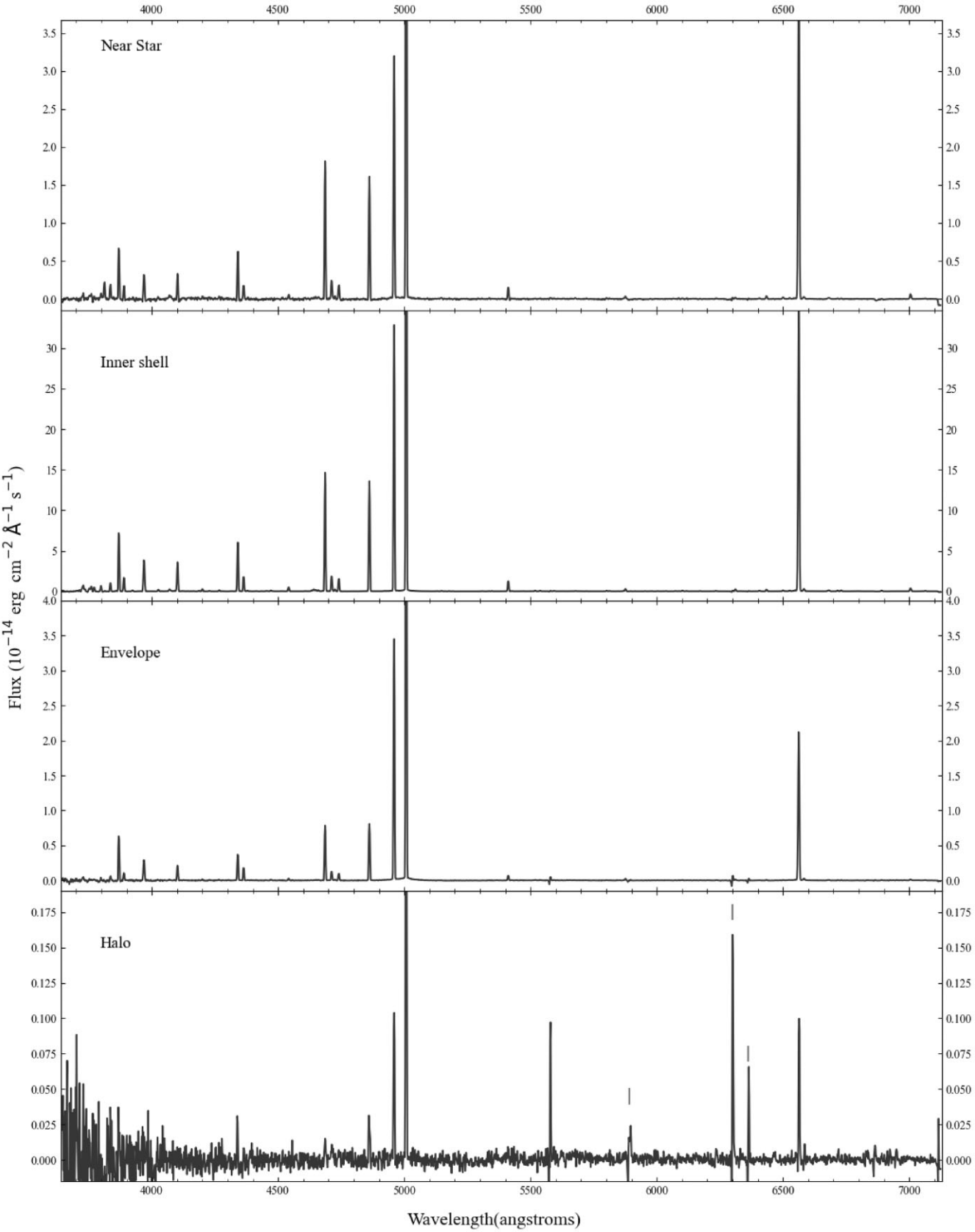

Figure A1. Spectra of NGC 2022 extracted from the apertures shown in Fig. 1. Sky lines are marked by red ticks in the spectrum of the halo to avoid confusing them with nebular emission lines.

This paper has been typeset from a TEX/LATEX file prepared by the author.